ADVANCED SCIENCE
Open Access

Supporting Information

for *Adv. Sci.*, DOI 10.1002/advs.202303696

A Stress Self-Adaptive Silicon/Carbon "Ordered Structures" to Suppress the Electro-Chemo-Mechanical Failure: Piezo-Electrochemistry and Piezo-Ionic Dynamics

Hongshun Zhao, Kang Liang, Shijie Wang, Zhengping Ding, Xiaobing Huang, Wenkai Chen, Yurong Ren and Jianbin Li**

Supporting Information

A stress self-adaptive silicon/carbon "ordered structures" to suppress the electro-chemo-mechanical failure: piezo-electrochemistry and piezo-ionic dynamics

Hongshun Zhao, Kang Liang, Shijie Wang, Zhengping Ding, Xiaobing Huang, Wenkai Chen, Yurong Ren and Jianbin Li**

H. Zhao, K. Liang, S. Wang, Z. Ding, Y. Ren, J. Li

School of Materials Science and Engineering

Jiangsu Province Engineering Research Center of Intelligent Manufacturing Technology for the New Energy Vehicle Power Battery

Changzhou Key Laboratory of Intelligent Manufacturing and Advanced Technology for Power Battery

Changzhou University

Changzhou 213164, P. R. China

E-mail: ryrchem@cczu.edu.cn; jianbinchem@cczu.edu.cn

X. Huang

College of Chemistry and Materials Engineering

Hunan University of Arts and Science

Changde 415000, P. R. China

W. Chen

Department of Chemistry

Fuzhou University

Fuzhou 350116, P. R. China

1 Experimental section

1.1 Synthesis of Si@ZIF-8 materials

To synthesise the Si@ZIF-8 precursor, a solution was prepared by dissolving 6.16 g of 2-methylimidazole (Sigma-Aldrich) and 50 mg of Si NPs (Sigma-Aldrich) in 100 ml methanol under ultrasonication for 30 min and another solution was prepared by dissolving 5.82 g of $Co(NO_3)_2•6H_2O$ (Sigma-Aldrich) in 100 ml methanol. These solutions were then mixed under constant stirring at room temperature for 24 h to form a Si@ZIF-67 suspension solution. Then, the Si@ZIF-67 powder was collected from the suspension solution by centrifugation, washing with methanol and vacuum drying.

1.2 Synthesis of Si/C@CNTs materials

The powder forms of Si@ZIF-8 precursors were first reduced under Ar/H_2 flow at 350℃ for 2 h and then carbonised at 700℃ for 3 h. This was followed by a thermal treatment process by replacing the Ar/H_2 gas with pure Ar at 930℃ for 2 h to remove Co.

1.3 Synthesis of BNT materials

Bismuth nitrate pentahydrate ($Bi(NO_3)_3·5H_2O$, Sinopharm, China, ≥99.0%), tetrabutyl titanate ($Ti(OC_4H_9)_4$, Sinopharm, China, ≥98.0%), sodium hydroxide (NaOH, Sinopharm, China, ≥96.0%) were used as raw materials for hydrothermal reactions. In a typical synthetic procedure, firstly, 5.82 g $Bi(NO_3)_3$ $5H_2O$ was dissolved in 60 ml distilled water and stirred for 15 min. Secondly, 8.16 ml $Ti(OC_4H_9)_4$ solution was added into the $Bi(NO_3)_3$ $5H_2O$ solution drop by drop, then continually stirred for 30 min. Thirdly, NaOH with a concentration of 12 M was added into the solution where suspensions were subsequently formed. The suspensions were continually stirred for 30 min. The as-prepared mixture was poured into a 100 ml Teflon-lined autoclave with a filling capacity of 60% and hydrothermally treated at 150°C for 12 h. After the reaction, the autoclave was cooled down to room temperature in air. Finally, the products were collected and washed by distilled water and freeze-dried for 72 h.

1.4 Synthesis of Si/C@CNTs@BNT materials

The Si/C@CNTs@BNT nanocomposites were prepared using a high-energy ball-milling process. For the preparation of Si/C@CNTs@BNT, BNT was directly added into Si/C@CNTs material, and then ball-milled for 1 h with the mass ratio of 9:1 at 1600 rpm.

1.5 Materials characterizations

Crystal structure of all samples were characterized by powder X-ray diffraction (XRD) with Cu K_α radiation (D/MAX2500, Rigaku, Japan), and the Rietveld refinement of XRD patterns was achieved by the Fullprof program; the surface morphology and structure were characterized by scanning electron microscope (SEM, JSM-6360, JEOL, Japan) and high resolution transmission electron microscope (TEM, JEOL2100, JEOL, Japan); X-ray photoelectron spectroscopy (XPS, PHI 5000 VersaProde III, LUVAC-PHI, Japan) was applied for elemental analysis and valence determination; The specific surface area were further explored Brunauer-Emmett-Teller (BET, ASAP2460, N_2-adsoprtion/desorption). The piezoelectric effect of as-prepared sample was measured by piezoelectric force microscopy (PFM, Oxford MFP3D). The Young's modulus of sample was determined by atomic force microscope (AFM, Bruker Senta, CA, USA). Dual-beam FIB (Helios c Nanolab 660) was performed for scanning the particles in the cross-sectional view. Additionally, in situ XRD patterns of cathode electrodes were tested in the specially made chamber (Beijing scistar technology Co. Ltd) with the step of 0.013° in the scanning range of 10-55°.

1.6 Electrochemical measurements

The samples were mixed with Super P and sodium carboxymethyl cellulose (CMC) at the weight ratio of 8:1:1 in distilled water to form a slurry, which was coated on Cu foil. After vacuum drying at 80 °C for 10 h, the electrodes were assembled into 2032-type coin cells in a glovebox (MBC-Labstar) filled with ultra-high-purity argon. The mass loading of the electrode materials on Cu foil was about 1.35 mg cm^{-2}. The specific capacity is calculated based on the weight of electrode materials. In the coin cells, Li metal foil and Celgard 2400 film were used as the anode and separator, respectively, and the electrolyte was 1 M $LiPF_6$ in ethylene

carbonate/dimethyl carbonate (1:1 v/v) with 10wt% fluoroethylene carbonate. The galvanostatic charge/discharge performances of the electrodes were conducted on a NEWARE battery tester. Cyclic voltammetry (CV) and electrochemical impedance spectroscopy (EIS, frequency range: 100 kHz to 0.01 Hz) both were tested with an electrochemical workstation (CHI604E, CH Instruments).

1.7. Calculation method

All the calculations are performed in the framework of the density functional theory with the projector augmented plane-wave method, as implemented in the Vienna ab initio simulation package. The generalized gradient approximation proposed by Perdew, Burke, and Ernzerhof is selected for the exchange-correlation potential. The long range van der Waals interaction is described by the DFT-D2 approach. The cut-off energy for plane wave is set to 500 eV. The energy criterion is set to 10^{-5} eV in iterative solution of the Kohn-Sham equation. A vacuum layer of more than 15 Å is added perpendicular to the sheet to avoid artificial interaction between periodic images. The Brillouin zone integration is performed using a 4×4×1 k-mesh. All the structures are relaxed until the residual forces on the atoms have declined to less than 0.01 eV/Å.

.

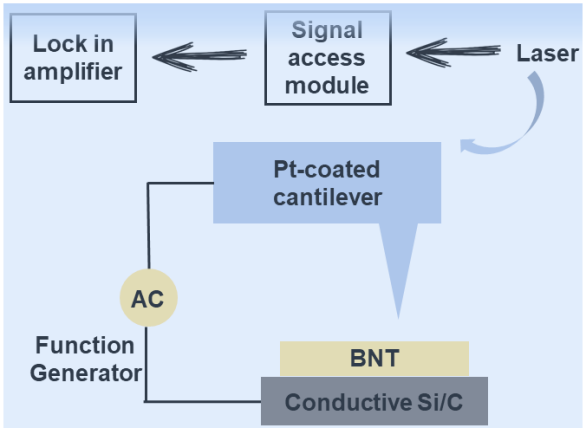

Figure S1. Standard PFM working program.

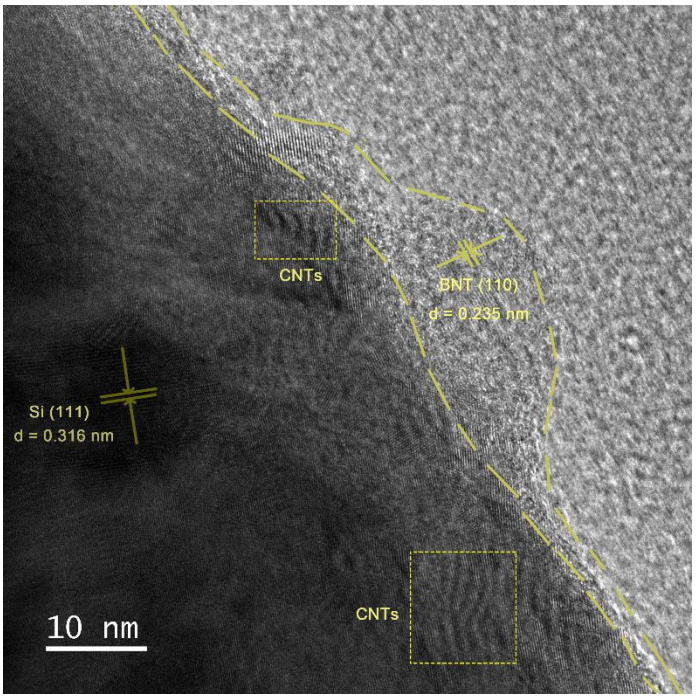

Figure S2. HRTEM pattern of the Si/C@CNTs@BNT sample.

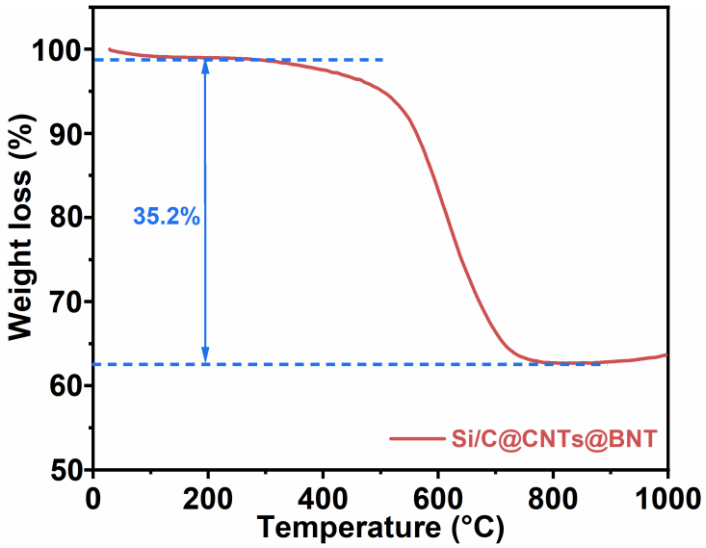

Figure S3. TGA curve of Si/C@CNTs@BNT sample.

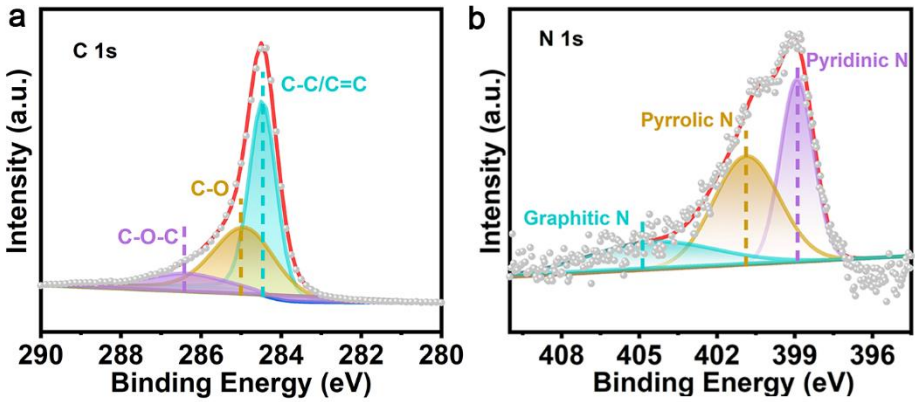

Figure S4. High-resolution (a) C 1s and (b) N 1s XPS spectrum for Si/C@CNTs material.

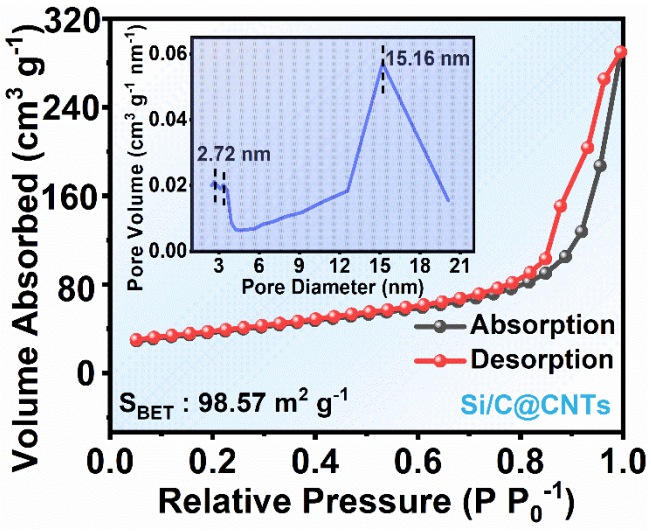

Figure S5. N_2 adsorption/desorption isotherm of Si/C@CNTs material.

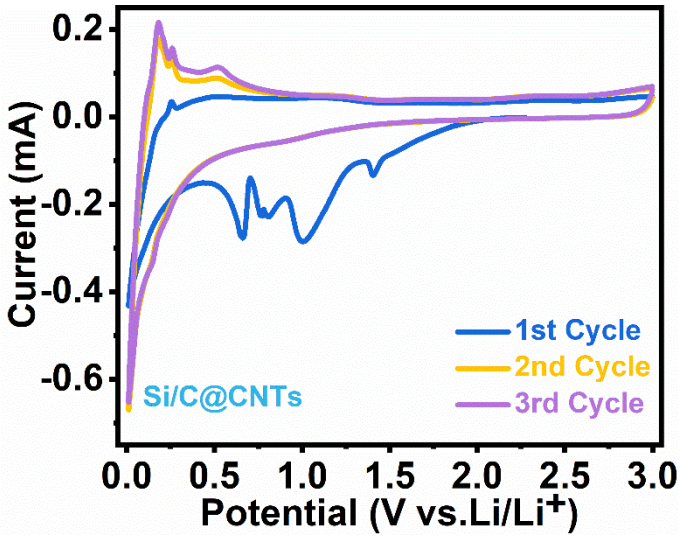

Figure S6. Initial three CV plots of Si/C@CNTs material.

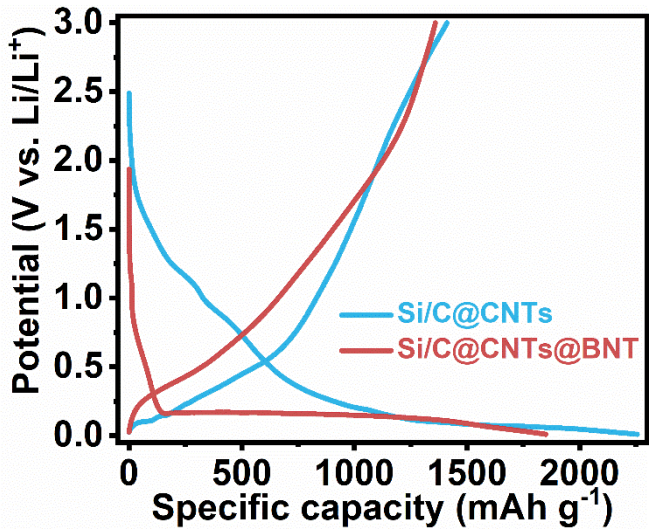

Figure S7. Initial discharge-charge curves of Si/C@CNTs and Si/C@CNTs@BNT material.

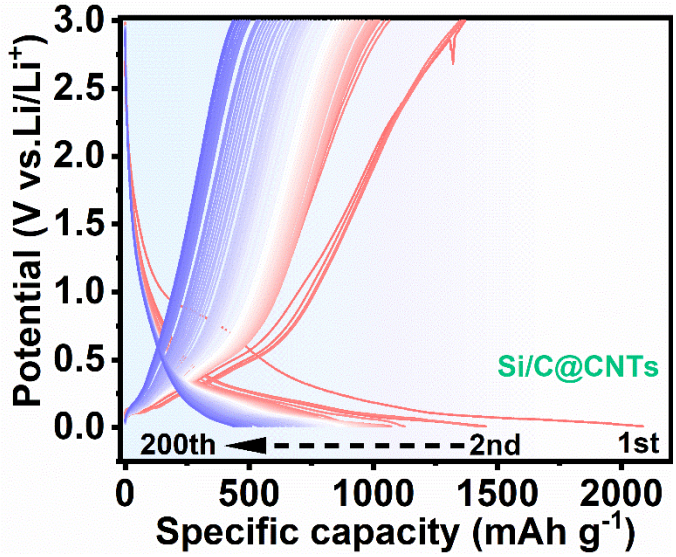

Figure S8. Typical discharge-charge voltage profiles of Si/C@CNTs material.

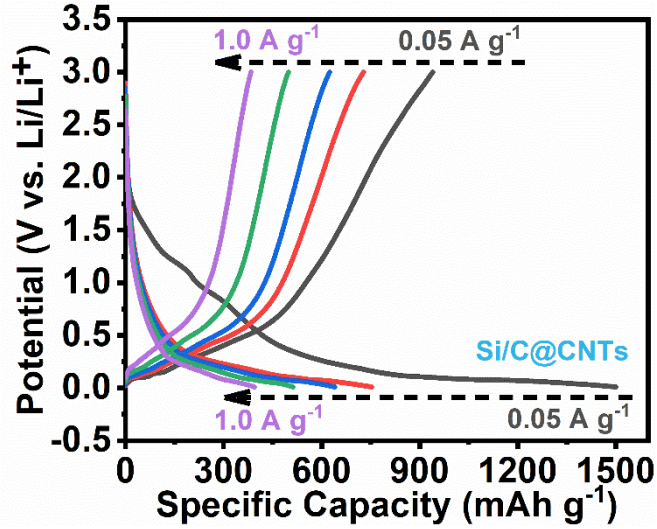

Figure S9. Charge-discharge curves of the Si/C@CNTs material anode under different current rates.

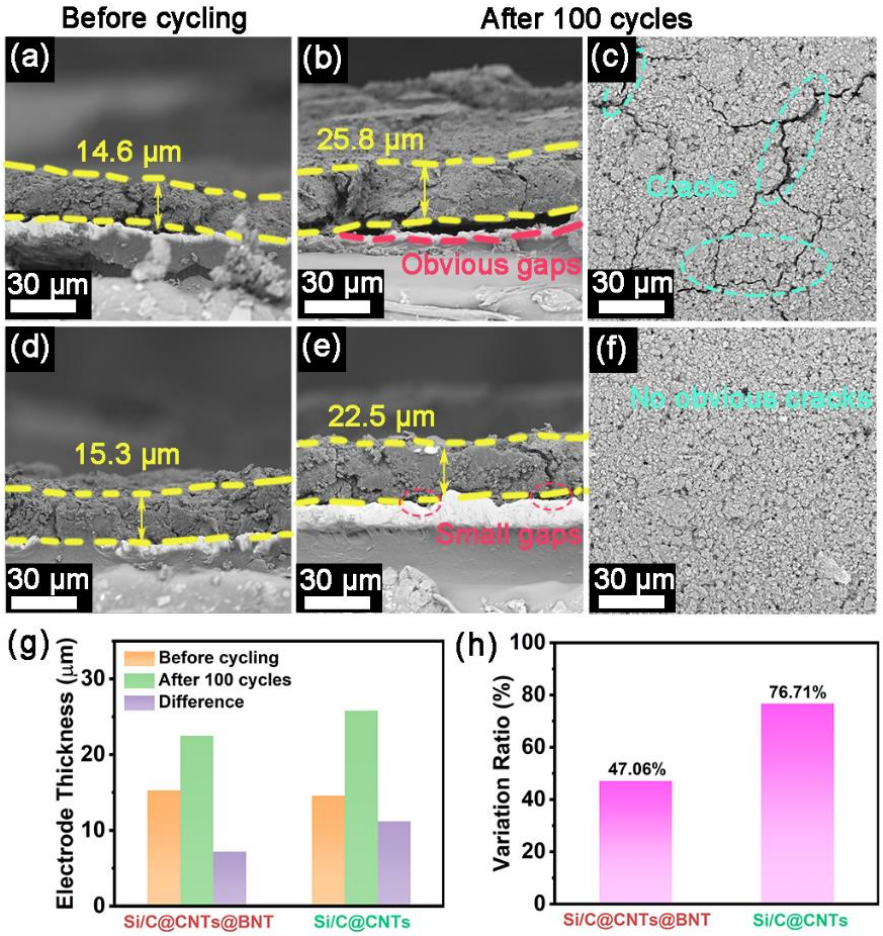

Figure S10. Cross-sectional SEM images of (a, b) Si/C@CNTs and (d, e) Si/C@CNTs@BNT before and after 100 cycles. SEM images of (c) Si/C@CNTs and (f) Si/C@CNTs@BNT electrode surface after 100 cycles. (g) Charting the electrodes' thickness variation before cycling and after 100 cycles. (h) the corresponding percentage change in electrode thickness.

Notes: In order to compare the volume effect and its surface morphology changes before and after cycling, we performed SEM characterization of the cross-sections of Si/C@CNTs and Si/C@CNTs@BNT electrodes before and after 100 cycles. As shown in Figure S10a and b, the thickness of the active material on the Si/C@CNTs pole piece before cycling is 14.6 μm, and after 100 cycles, the thickness of the active material on the pole piece is about 25.8 μm, and the volume expansion rate is about 76.71%. The phenomenon of falling off, and obvious cracks appeared on the surface of the pole piece due to the large volume expansion (Figure S10c), which is also one of the reasons for the rapid decay of battery capacity or even failure. In contrast, after calculation, the Si/C@CNTs@BNT anode has a volume expansion rate of about

47.06% before and after cycling (Figure S10d and e), and there is no gap between the electrode material and the current collector copper foil. There is obvious peeling off, and there are no obvious cracks on the surface of the electrode sheet (Figure S10f). These all indicate that the composite of piezoelectric material BNT can obviously "absorb" the volume expansion stress of silicon particles (Figure S10g and h). The mechanical stress generated by the alloying reaction induces the BNT piezoelectric material to generate a local electric field to improve the lithium ion transport performance, and at the same time relieve the volume expansion caused by the alloying reaction, thereby improving the material electrode reaction kinetics; in addition, during charging and Under the discharge DC electric field, interfacial polarization is generated between the ferroelectric layers. This interfacial effect accelerates the reaction kinetics of Li ions. This polarization may attract negative charges to the interface on the BNT side, thereby promoting the positively charged Li^+ rapid de-intercalation.

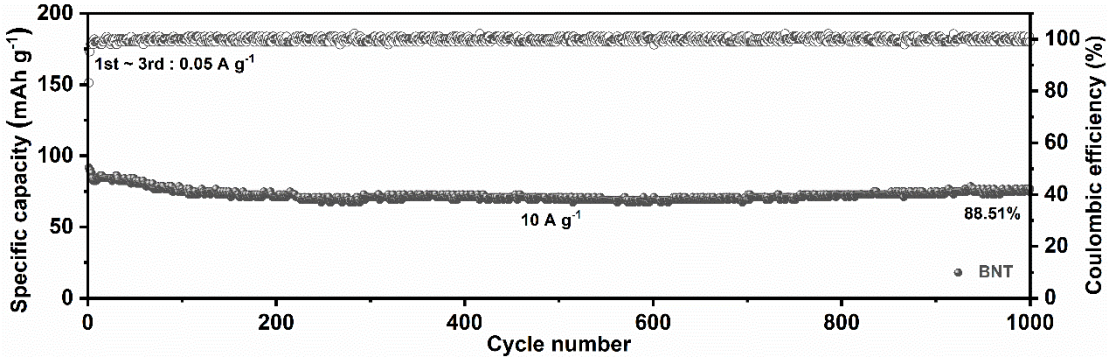

Figure S11. Long-term cycling performance of BNT at 10 A g^{-1}.

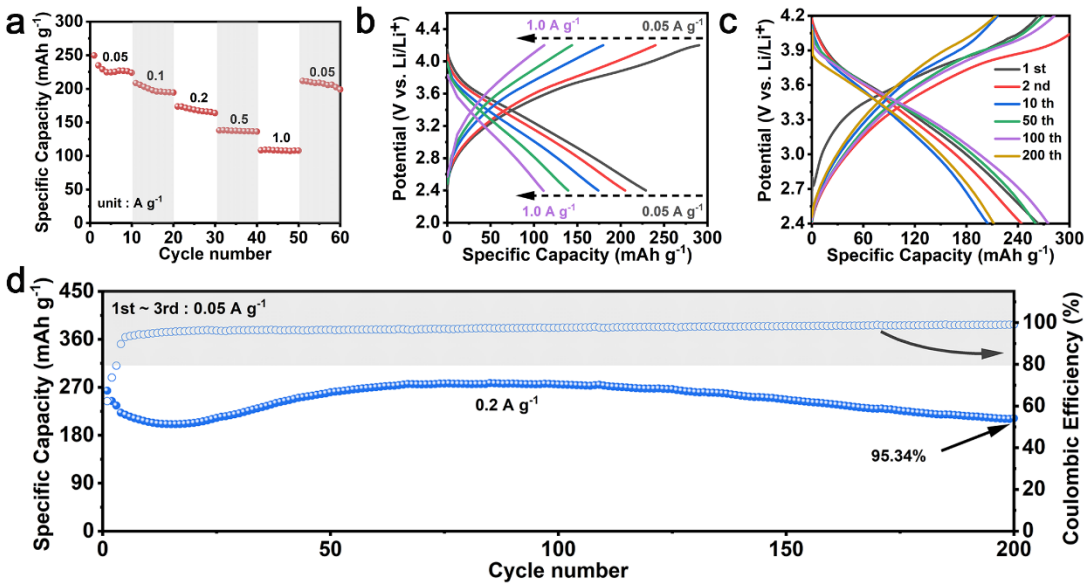

Figure S12. (a) Rate performance of Si/C@CNTs@BNT|$LiNi_{0.8}Co_{0.1}Mn_{0.1}O_2$ full cell at 0.05 ~ 1.0 A g^{-1}. (b) Discharge-charge voltage curves under different current densities. (c) Typical discharge-charge voltage profiles and (d) Cycling performance at 0.2 A g^{-1}.

Notes: To show the practical application of the as-reported anode, a full cell (Figure S12) was fabricated with Si/C@CNTs@BNT anode and $LiNi_{0.8}Co_{0.1}Mn_{0.1}O_2$ cathode. Figure S9a depicts impressive capacities of 218, 205, 173, 142 and 118 mAh g^{-1} at varied rates of 0.05~1.0 A g^{-1}. Besides, the full cell of Si/C@CNTs@BNT|$LiNi_{0.8}Co_{0.1}Mn_{0.1}O_2$ has a specific capacity of 202 mAh g^{-1} at 0.2 A g^{-1} and stable cycling after 200 cycles. Such findings confirm that the Si/C@CNTs@BNT electrode is a potential anode for LIBs.

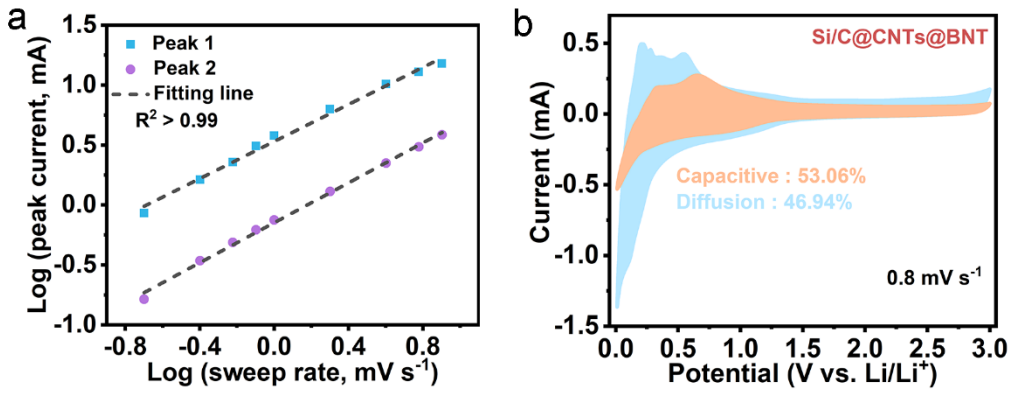

Figure S13. (a) Linear relationship of log (*v*) and log (*i*). (b) The pseudocapacitive contribution of the Si/C@CNTs@BNT sample at 0.8 mV s^{-1}.

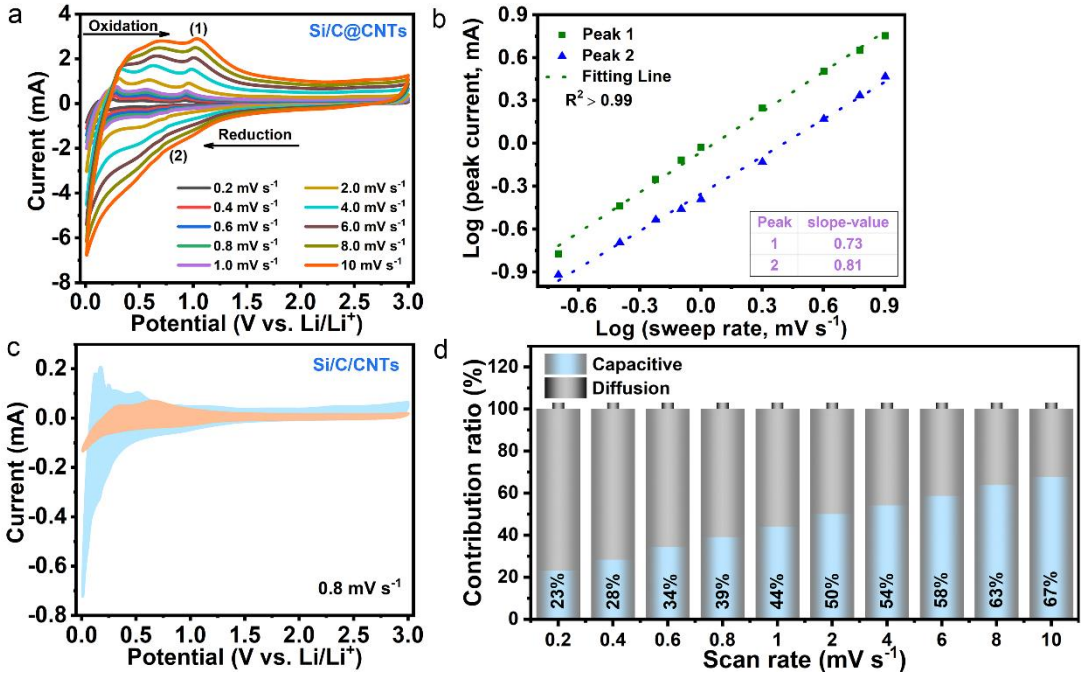

Figure S14. (a) CVs at various scan rates of Si/C@CNTs. (b) Linear relationship of log (v) and log (i). (c) The pseudocapacitive contribution of the Si/C@CNTs sample at 0.8 mV s^{-1}. (d) Percentage of pseudocapacitance contributions of Si/C@CNTs sample.

Notes: All of the CV plots in Figure 5f have near peak presentations and placements, confirming the electrode's weak polarization. In reality, capacitance/pseudocapacitance or intercalation capacity contributed to the total stored charges. It can be further analyzed according to equation (1) and (2):

$$i = av^b \quad (1)$$

$$\log (i) = b \log (v) + \log (a) \quad (2)$$

where i is the current density; v is the sweep speed; a and b are adjustable parameters. Several different cathodic (0.402 V and 0.781 V)/anodic (0.723 V) peaks were chosen to calculate b values that can be used to determine the lithium storage mechanism. The calculated b value can be used to determine the lithium storage mechanism of the composite electrode material. In general, b = 0.5 represents a diffusion-controlled lithium storage mechanism, while b = 1 represents a capacitive process (i.e., pseudocapacitance when Faraday reactions are involved). According to the calculation, the b-values of the two peaks are 0.726 and 0.738, respectively (Figure S13a), indicating that the overall lithium storage process of the composite electrode material is jointly determined by the diffusion control and the pseudocapacitive effect.

Furthermore, equation (3) is used to calculate the pseudocapacitance contribution:

$$i(v) = k_1 v + k_2 v^{0.5} \quad (3)$$

Among them, $k_1 v$ and $k_2 v^{0.5}$ correspond to capacitance and diffusion capacitance, respectively. At 0.8 mV s^{-1} (Figure S13b), the capacitive contribution accounts for 64.91% of the total capacity of Si/C@CNTs@BNT. And with the increase of the scan speed, the proportion of the capacitance contributed by the capacitive contribution also increased, and when the scan speed increased to 10 mV s^{-1}, the capacitive contribution reached the maximum value of 97.32% (Figure 5g).

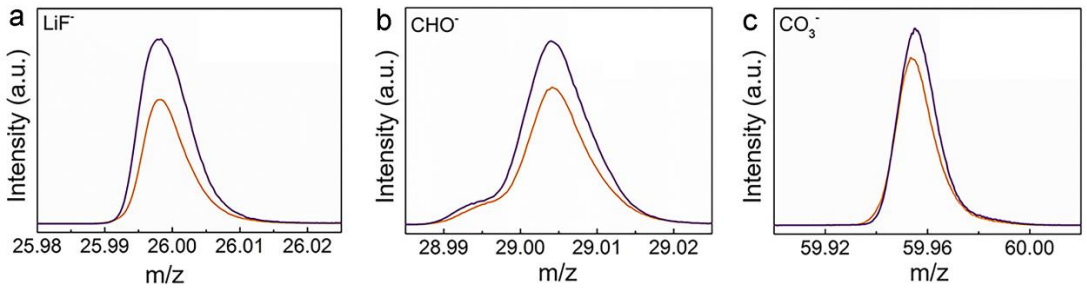

Figure S15. ToF-SIMS spectra of secondary ion fragments (a) LiF^-, (b) CHO^-, (c) CO_3^- collected from the Si/C@CNTs@BNT (Orange lines) and Si/C@CNTs (Purple lines) anodes after five cycles.

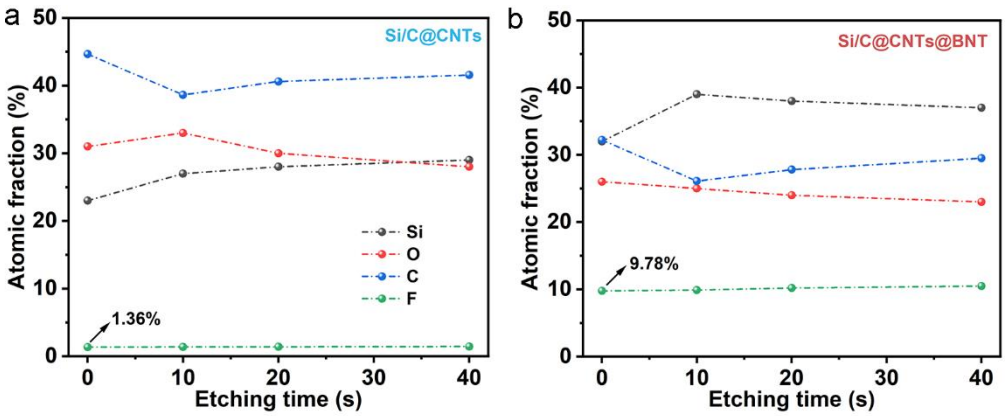

Figure S16. Time evolution of the atomic ratio of the Si, C, O, and F signals of the SEIs after different etching times on (a) Si/C@CNTs and (b) Si/C@CNTs@BNT electrodes after 40 cycles.

Notes: To further illustrate the structures of SEIs, the XPS spectra of Si/C@CNTs and Si/C@CNTs@BNT after 40 cycles were obtained with Ar^+ sputtering depth profiling. As shown in Figure S15a and b, for Si/C@CNTs@BNT, as we approach the SEI/electrode surface by increasing sputtering time, the carbon content decreases, while the fluorine content increases from 9.78 to 10.50% after 40 s of sputtering in comparison to an inconspicuous increase (from 1.36 to 1.45%) for Si/C@CNTs, indicating a gradually diminished organic component and increased LiF, implying that Si/C@CNTs@BNT achieves a LiF-rich SEI due to the FEC additive.

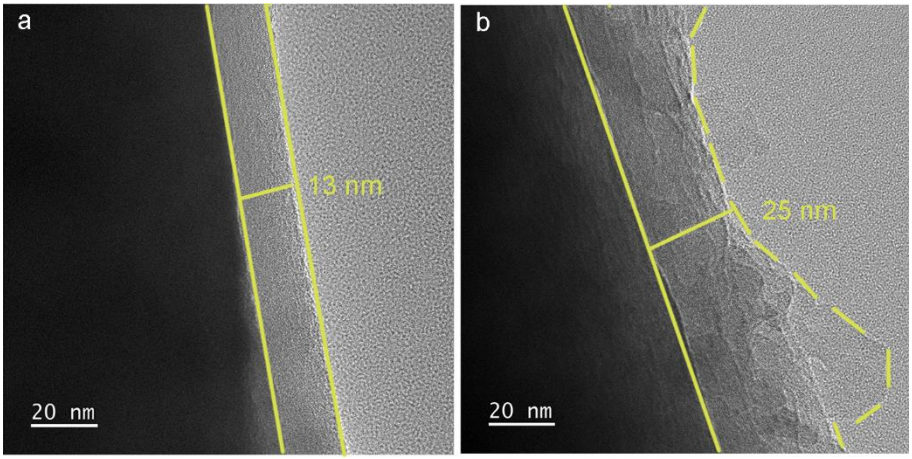

Figure S17. TEM images of (a) Si/C@CNTs@BNT and (b) Si/C@CNTs after 100 cycles.

The solid electrolyte interphase (SEI) layer on the surface of Si/C@CNTs@BNT and Si/C@CNTs electrodes after 100 cycles were further observed by TEM. From Figure S16a, it reveals that the Si/C@CNTs@BNT electrode is coated with a thinner and smooth interfacial SEI of about 13 nm, while the cycled Si/C@CNTs electrode generates a thick and uneven SEI layer (Figure S16b).

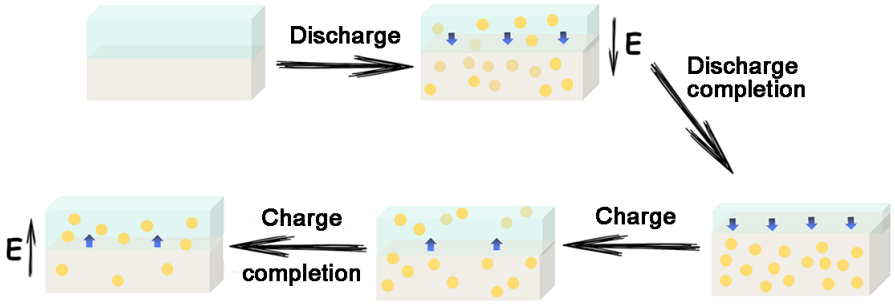

Figure S18. Schematic diagram of surface coating structure of anode material for LIBs with piezoelectric effect.

Notes: The analysis of the above experimental results shows that the piezoelectric material BNT as the coating layer can induce a local electric field due to the volume effect of the silicon-carbon material during charge and discharge, and regulate the lithium ion transport at the interface of the silicon-carbon anode material, so as to effectively improve the structural stability and electrochemical cycle performance of the composite material. Figure S17 is a schematic diagram of the surface coating structure of the negative electrode material of a lithium-ion battery with piezoelectric effect. A represents the state before discharge, the upper layer is the BNT piezoelectric modified layer, and the lower layer is the Si/C negative electrode composite layer. B represents the state in the discharge process, in which the embedded ball represents lithium ion. When the discharge starts, lithium ion is embedded into the negative electrode material from the electrolyte, and with the occurrence of volume effect (the lower part becomes wider), the piezoelectric coating layer (the upper part) is squeezed, and the piezopoietic potential (arrow in the lower part) is generated in the coating layer, and the direction of the piezopoietic potential is downward. The diffusion direction is the same as that of lithium ions; C represents the state at the end of discharge. When the discharge ends, all lithium ions in the negative electrode material are embedded, and the volume effect is the most significant (the lower part is the largest). At this time, the BNT piezoelectric modified layer is subjected to the largest upward mechanical stress, corresponding to the maximum piezopoietic potential in the coating layer at this time, and the direction of piezopoietic potential at this time

is the same as the direction of lithium ion diffusion. Greatly promote the diffusion and migration of lithium ions; On the other hand, E represents the charging state, when the charging starts, the lithium ions begin to release through the negative electrode material (the upper part) to the piezoelectric coating (the lower part), and the Si/C negative electrode volume gradually returns to the original size, and the mechanical stress acting on the BNT gradually decreases. However, the gradual disappearance of the external force does not mean the disappearance of the piezoelectric effect, and the piezoelectric modified layer of BNT itself may have a tendency to prevent the disappearance of the piezoelectric effect, forming a reverse piezoelectric electric field, which just promotes the rapid migration of lithium ions from the negative electrode and diffusion to the positive electrode. The volume effect gradually decreases (the lower part becomes smaller and smaller), and the pressure on the piezoelectric coating decreases, corresponding to the decrease of the internal piezoelectric potential, but the direction is still upward, consistent with the direction of the diffusion of lithium ions and the direction of the applied electric field. At the end of the discharge, most of the lithium ions return to the positive electrode (most of the balls in the upper part), and some of them cannot return, corresponding to the negative electrode material cannot return to the original position, compared with the beginning, there is still some expansion (the upper part is slightly larger than the upper part of B), and there is still pressure on the coating layer (the lower part), corresponding to the minimum piezoelectric potential at this time. The direction is consistent with the direction of lithium ion diffusion and the direction of applied electric field.

Table S1. Electrochemical performance comparisons of lithium storage performance of recently reported Si-based anodes.

Sample	lithium storage capability	Reference
P-Si/C@C microspheres	1003 mAh g^{-1} at 0.1 A g^{-1} (100 cycles)	S1
	708 mAh g^{-1} at 1.0 A g^{-1} (1000 cycles)	
multi-Si-void@SiO_2	1458 mAh g^{-1} at 0.1 A g^{-1} (200 cycles)	S2
nanoparticles	1258 mAh g^{-1} at 1.2 A g^{-1} (400 cycles)	
Si NDs⊂MDN	1327 mAh g^{-1} at 0.1 A g^{-1} (100 cycles)	S3
	1120 mAh g^{-1} at 1.0 A g^{-1} (1100 cycles)	
Si@zincone/TiO_2	1983 mAh g^{-1} at 0.2 A g^{-1} (100 cycles)	S4
	890 mAh g^{-1} at 2.0 A g^{-1} (1000 cycles)	
Si-C/G-S nanoparticles	446 mAh g^{-1} at 0.5 A g^{-1} (200 cycles)	S5
H-TiO_x/SiO_x@C	978 mAh g^{-1} at 1.0 A g^{-1} (1000 cycles)	S6
nanoparticles	780 mAh g^{-1} at 2.0 A g^{-1} (600 cycles)	
HD-Si@$Ti_3C_2T_x$@G	2123 mAh g^{-1} at 0.1 A g^{-1} (150 cycles)	S7
	1120 mAh g^{-1} at 1.0 A g^{-1} (800 cycles)	
Si-C/TiO_2 composites	919 mAh g^{-1} at 0.8 A g^{-1} (900 cycles)	S8
	593 mAh g^{-1} at 3.0 A g^{-1} (1500 cycles)	
This work	2084 mAh g^{-1} at 0.2 A g^{-1} (200 cycles)	-
	838 mAh g^{-1} at 10 A g^{-1} (1000 cycles)	

[S1] W. An, P. He, Z. Che, C. Xiao, E. Guo, C. Pang, X. He, J. Ren, G. Yuan, N. Du, D. Yang, D. L. Peng and Q. Zhang, *ACS Appl. Mater. Interfaces*, 2022, **14**, 10308-10318.

[S2] X. Bi, T. Tang, X. Shi, X. Ge, W. Wu, Z. Zhang and J. Wang, *Small*, 2022, **18**, 2200796.

[S3] B. Chen, L. Chen, L. Zu, Y. Feng, Q. Su, C. Zhang and J. Yang, *Adv. Mater.*, 2022, **34**, 2200894.

[S4] J. B. Fang, Y. Q. Cao, S. Z. Chang, F. R. Teng, D. Wu and A. D. Li, *Adv. Funct. Mater.*, 2021, **32**, 2109682.

[S5] J. Gao, S. Zuo, H. Liu, Q. Jiang, C. Wang, H. Yin, Z. Wang and J. Wang, *J. Colloid. Interface Sci.*, 2022, **624**, 555-563.

[S6] J. Ge, T. Guo, H. Shen, F. Zhou, Y. Li, N. Yuan, W. Yang, Z. Wang, Y. Xu, J. Zhang and Y. A. Wu, *J. Power Sources*, 2023, **555**, 232357.

[S7] Z. Liu, D. Lu, W. Wang, L. Yue, J. Zhu, L. Zhao, H. Zheng, J. Wang and Y. Li, *ACS Nano*, 2022, **16**, 4642-4653.

[S8] C. Xu, L. Shen, W. Zhang, Y. Huang, Z. Sun, G. Zhao, Y. Lin, Q. Zhang, Z. Huang and J. Li, *Energy Stor. Mater.*, 2023, **56**, 319-330.

Supplementary Note 1

The diffusion coefficient (D) in Si/C@CNTs, Si/C@CNTs@BNT electrodes can be calculated from the GITT potential profiles through Fick's second law according to the following equation:

$$D = \frac{4}{\pi\tau}\left(\frac{m_B v_M}{M_B S}\right)^2\left(\frac{\Delta E_s}{\Delta E_t}\right)^2$$

where τ represents the duration of the current pulse, stands for the electrode active material mass, S is the geometric area of the electrode, ΔE_s represents the quasi-thermodynamic equilibrium potential difference before and after the current pulse, ΔE_t is the potential difference during current pulse, V_M is the molar volume of the samples, and M_B is the molar mass of carbon. The result of M_B/V_M can be calculated from the density of the carbon material based on the following equation:

$$\rho = \frac{1}{v_{total} + \frac{1}{\rho_{TiO_2}}}$$

where ρ (g cm^{-3}) represents the density of the Si/C materials, V_{total} (cm^3 g^{-1}) represents the total pore volume which comes from the N_2 absorption/desorption isotherms, ρ_{Si} represents the known true density of Si/C materials.

Supplementary Note 2

Formula S1:

$$\varepsilon=\frac{\Delta d}{d} \quad (1)$$

here ε was the strain produced by the interplanar spacing, Δd was the change in interplanar spacing, and d is the interplanar spacing.

Formula S2:

$$E=\frac{\sigma}{\varepsilon} \quad (2)$$

here E is the Young's modulus of the samples, σ is the stress, and ε is the strain.